ACS NANO
Cite This: ACS Nano 2018, 12, 1712−1719
www.acsnano.org
ARTICLE

High Anisotropy in Tubular Layered Exfoliated KP_{15}

Nan Tian,[†,‡,▽] Yanhan Yang,[†,§,▽] Danmin Liu,*[,†,‡] Xuelu Liu,[∥] Ping-Heng Tan,[∥] Dong Zhang,[∥] Kai Chang,[∥] Hui Li,[†,‡] Minjian Zhao,[⊥] Jian Rong Li,[⊥] Xu Tang,[#] Dandan Zhang,[†,‡] Zhenlu Zhang,[†,‡] Weiqiang Xiao,[†,‡] Hui Yan,[†,§] and Yongzhe Zhang*[,†,§]

[†]Beijing Key Laboratory of Microstructure and Properties of Advanced Material, Beijing University of Technology, 100, Pingleyuan, Chaoyang District, Beijing, 100124, China

[‡]Institute of Microstructure and Property of Advanced Materials, Beijing University of Technology, 100, Pingleyuan, Chaoyang District, Beijing, 100124, China

[§]College of Materials Science and Engineering, Beijing University of Technology, 100, Pingleyuan, Chaoyang District, Beijing, 100124, China

[∥]State Key Laboratory of Superlattices and Microstructures, Institute of Semiconductors, Chinese Academy of Sciences, 35, Qinghua East Road, Haidian District, Beijing, 100083, China

[⊥]Beijing Key Laboratory for Green Catalysis and Separation, Department of Chemistry and Chemical Engineering, College of Environmental and Energy Engineering, Beijing University of Technology, 100 Pingleyuan, Chaoyang District, Beijing, 100124, China

[#]Electron Microscopy Laboratory, Institute of Geology and Geophysics, Chinese Academy of Sciences (EML, IGGCAS), 19, Beitucheng West Road, Chaoyang District, Beijing, 100029, China

Supporting Information

ABSTRACT: Two-dimensional (2D) materials with high anisotropic properties, such as black phosphorus and ReS_2, show amazing potential for applications in future nanoelectronic and optoelectronic devices. However, degradation of black phosphorus under ambient conditions and the expensiveness of Re block their application. In this study, another layered material, KP_{15}, that has highly anisotropic properties was successfully prepared. The detailed crystal structure and electron-density distribution calculation reveal that KP_{15} exhibits an anisotropic layered structure with two rows of P tubes connected by K atoms that are antiparallel in a single layer. Outstanding chemical stability, angular dependence of the Raman response, excitation, and exciton emission at room temperature have been found in exfoliated KP_{15} nanoribbons. Importantly, the exciton emission at room temperature suggests the existence of a large exciton binding energy. Our results indicate that, because this layered material, KP_{15}, has high anisotropic properties and ultrachemical stability and is derived from abundant raw materials, it has great potential for applications in optoelectronic devices.

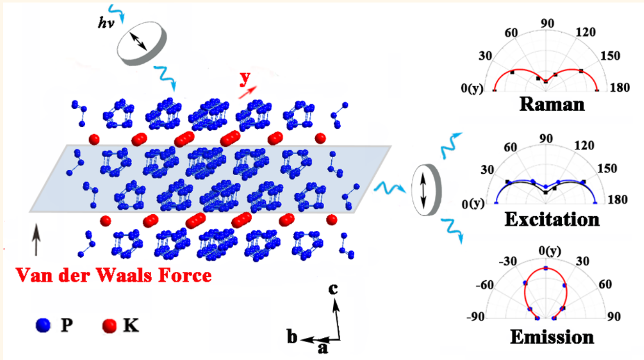

KEYWORDS: *KP_{15}, layered-like structure, anisotropy, anisotropic Raman response, anisotropic exciton emission, anisotropic excitation*

Research on 2D materials, including graphene,[1−5] TMDCs,[6−8] and insulating hexagonal boron nitride,[9−11] has increased sharply due to their rich physics and tremendous potential for application. However, the most studied 2D materials are isotropy, which stems from their highly symmetric lattice structures. Reducing the symmetry of the 2D lattice system could lead to high structural anisotropy and further cause a strong anisotropy of their electronic structures and optical properties. Such anisotropic 2D materials are promising for fabricating high performance electronic and optical devices, investigating hyperbolic 2D materials, and researching the magnetic performance of the nonsaturating magnetoresistance effect and unusual quantum Hall effects.[12−16] For example, based on the anisotropy of light responsiveness, 2D materials with low lattice structure, such as black phosphorus and ReS_2, can be directly used to develop

Received: November 26, 2017
Accepted: January 26, 2018
Published: January 27, 2018

DOI: 10.1021/acsnano.7b08368
ACS Nano 2018, 12, 1712−1719

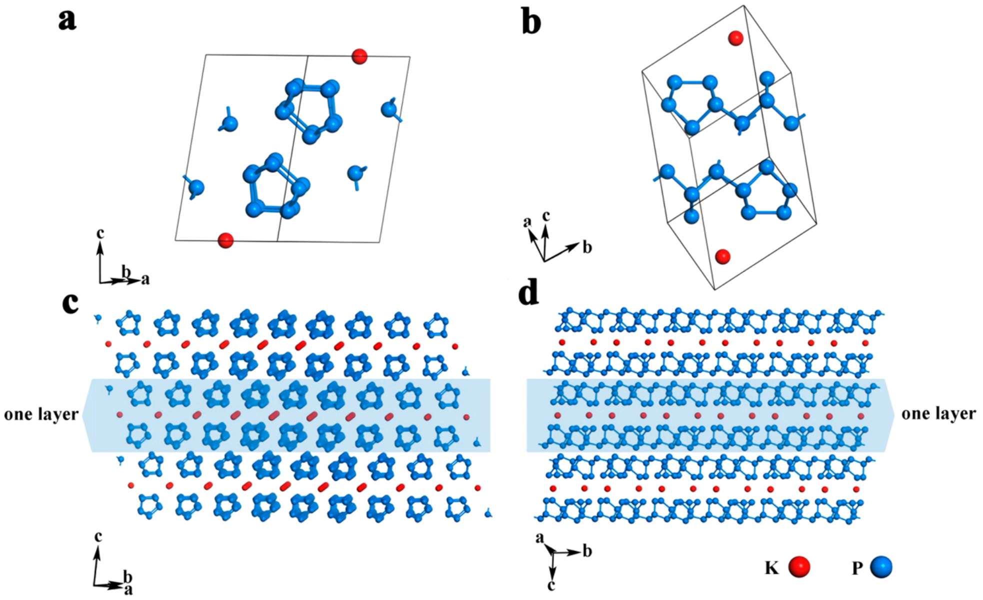

Figure 1. Crystal structure of KP_{15}. (a) Sectional view of a unit cell. (b) Side view of the unit cell. (c,d) Few layers of KP_{15}; one layer of KP_{15} has been marked by a light blue square.

ultrasmall volume polarization sensors.[17,18] Micro digital inverters that are based on the anisotropy of ReS_2 may now be able to meet the requirements for use in integrated circuits, and the microelectronic processors used in those micro digital inverters can be simplified.[19] Thus, 2D materials with high anisotropy can effectively increase the number of possible applications, but the development of 2D high in-plane anisotropic materials faces a challenge. Specifically, light-induced oxidation of black phosphorus causes it to degrade when exposed to the atmosphere,[20] and Re, the basic component element of ReS_2, is scarce and expensive.

KP_{15} was first synthesized by Schenering *et al.* in 1967.[21] Early research (prior to 1985) only reported the Raman, space group, unit cell parameters, and the low electric conductivity of bulk KP_{15}.[22,23] After that, the research on KP_{15} remained stagnant. Thus, its detailed crystal structure and anisotropy have not been studied. In this paper, single crystal X-ray diffraction first determined that KP_{15} is anisotropic phosphorus-rich alkaline phosphide consisting of antiparallel-arranged pentagonal phosphorus tubes connected by K atoms. Its electron-density distribution further showed that KP_{15} is a layered material with multiple types of chemical bonds. Its excellent chemical stability was confirmed by exposure to ambient conditions. KP_{15} nanoribbons were exfoliated, indicating that KP_{15} can be prepared as not only a 2D material but also a quasi-1D material. Because of that, extreme one-dimensional electronic and magnetic properties may be observed in KP_{15}.[24−27] Additionally, angular dependence of the Raman response, excitation, and exciton emission were observed in both exfoliated KP_{15} nanoribbons and micro-ribbons by angle-resolved polarized Raman and photoluminescence spectroscopy at room temperature, revealing an intrinsic anisotropy for KP_{15}. The observed exciton emission at room temperature also suggests a large exciton binding energy for KP_{15}. The intrinsic anisotropy and good chemical stability of KP_{15} suggest its promise for researching many-body physics and for developing electronic and optoelectronic devices in the future.

RESULTS AND DISCUSSION

To characterize the crystal structure of KP_{15}, single-crystal diffraction data were collected at room temperature. The KP_{15} crystal structure is shown in Figure 1 (crystal information can be seen in Table 1 and Tables S1−S3). The space group of the KP_{15} crystals in the triclinic crystal system is $P\bar{1}$ with lattice parameters a = 7.1506(6) Å, b = 9.1521(6) Å, c = 11.9392(13) Å, α = 89.594(7) °, β = 78.55(8) °, γ = 71.843(7) °. As shown in Figure 1, KP_{15} can be separated into parallel units. Each unit consists of two antiparallel rows of P (phosphorus) tubes. Four adjacent P tubes in one unit are coordinated by K (potassium). Each P tube can be separated into many $[P_{15}]^-$ cells. Within one $[P_{15}]^-$ cell, one P atom has two adjacent P atoms and the other 14 P atoms have three adjacent P atoms. That causes the

Table 1. Crystal Data and Structure Refinement for a KP_{15} Single Crystal

Formula sum	KP_{15}
Molar mass [g mol^{-1}]	50.36
Crystal system	triclinic
Space group	$P\bar{1}$(2)
a [Å]	7.1506(6)
b [Å]	9.1521(6)
c [Å]	11.9392(13)
α [°]	89.594(7)
β [°]	78.55(8)
γ [°]	71.843(7)
V [Å^3]	726.40(11)
Z	10
Calc. density [g cm^{-3}]	1.15115
Completeness [%]	85.4
Reflections collected/unique	4339/2501
Data/restraints/parameters	2501/0/161
Final R indices $R1$	0.0856
Goodness-of-fit on F^2	1.040
$wR2$	0.2136
Largest diff. peak and hole [e Å^{-1}]	3.638/−0.889

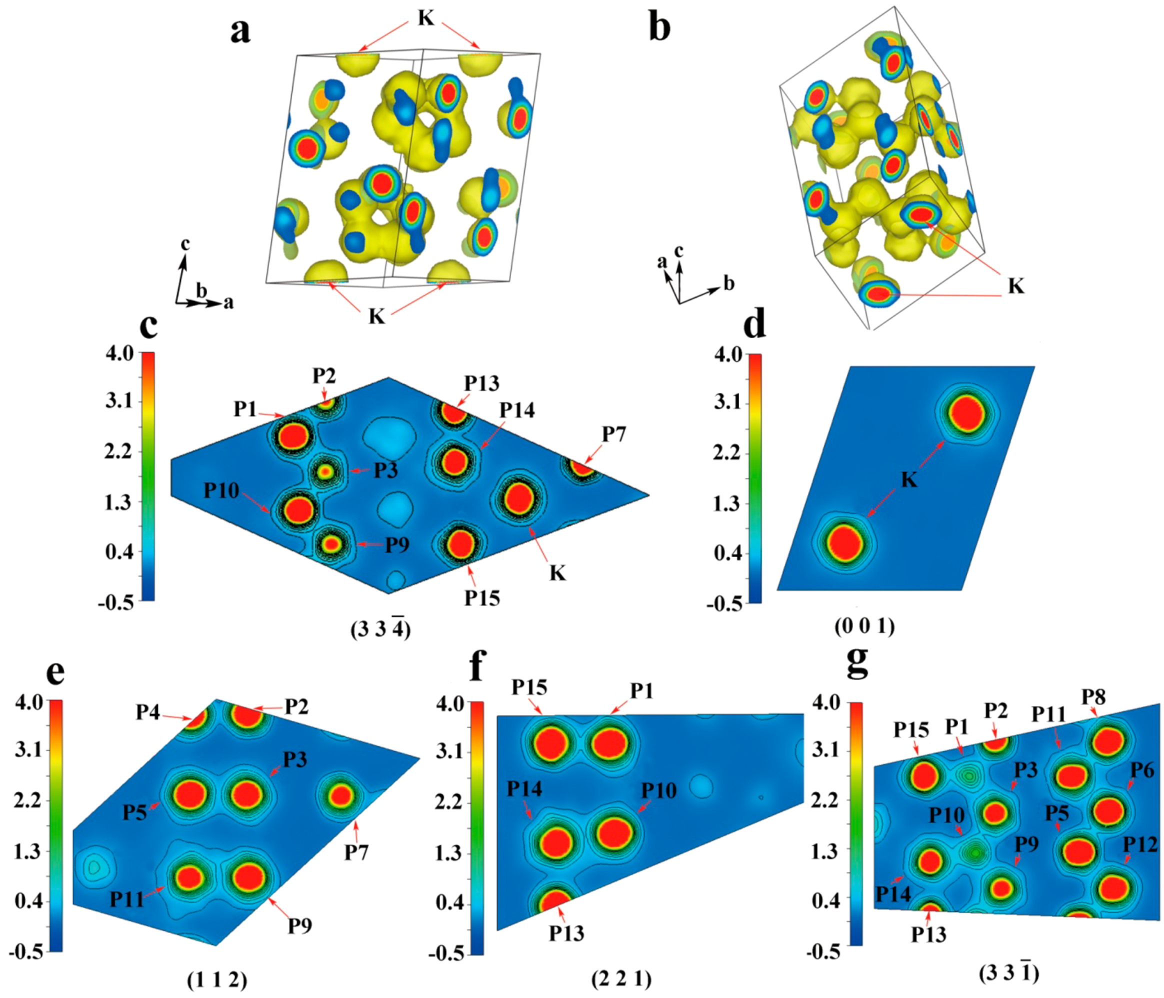

Figure 2. Electron density of KP_{15} calculated by MEM. (a) **Sectional view of the 3D EDD in KP_{15} cell unit.** (b) **Side view of the 3D EDD in KP_{15} cell unit.** (c−g) **Contour maps of the EDD on KP_{15} for the (3 3 $\bar{4}$), (0 0 1), (1 1 2), (2 2 1) and (33$\bar{1}$) planes. Distances from origin are as follows: 0.5, 0, 1.7, 1.65, and 1.9. Saturation levels are from 4 to −0.5. The contours are drawn every 0.2 e Å^{-3} in a range from 0.2 to 2.0 e Å^{-3}.**

$[P_{15}]^-$ cell to adopt a pentagonal arrangement in cross-section. This tubular phosphorus structure makes KP_{15} highly anisotropic.

An accurate method for determining the types of chemical bonds in KP_{15} is to calculate the electron-density distribution (EDD) from the structure factor data deduced from X-ray diffraction data by the maximum entropy method (MEM).[28,29] This method could be called the experimental method; the calculation process does not make any approximations, and the results are not disturbed by human factors. After refining single X-ray diffraction data, the structure factor data of KP_{15} can be obtained and the experimental EDD by the MEM is shown in Figure 2. 3D images of the EDD for the KP_{15} unit cell are shown in Figure 2a, 2b, and contour maps of the EDD corresponding to the (3 3 $\bar{4}$), (0 0 1), (1 1 2), (2 2 1), and (3 3$\bar{1}$) planes are shown in Figure 2c−g, respectively. In one P tube, the EDD around each P atom overlaps with the distribution around the adjacent P atoms (Figure 2d−g). Thus, the adjacent P atoms along the P tubes are all connected by covalent bonds. There is no overlap of EDD between adjacent P tubes, which means that the EDDs of adjacent P tubes are independent. The EDD around the K atoms is approximately spherical (Figure 2c, 2d). No overlap can be observed between K and P, so the K atoms appear to be connected to the P atoms by either ionic bonds or van der Waals interactions. Additionally, based on the high activity of metallic K and the growth temperature of KP_{15}, the K atoms cannot stay between the P tubes without gaining or losing electrons. Thus, we believe that the K atoms are connected to the P tubes by ionic bonds. The adjacent P tubes that are not connected by K atoms have no overlap of EDD, so van der Waals forces appear to be the main interaction between the layers. These findings reveal that KP_{15} is a type of layered material. The theoretical EDD of KP_{15}, which was obtained by first-principles calculations (Figure S3), also shows a similar result. KP_{15} is clearly a type of layered structure, which contains multiple types of bonds.

Mechanically exfoliated nanometer-sized KP_{15} was transferred to a silicon wafer covered with 300 nm SiO_2. The optical, AFM images and Raman results for the exfoliated KP_{15} are shown in Figure 3a−c. The thickness of the freshly exfoliated sample was as low as 20.6 nm. Moreover, all the cleaved KP_{15} samples presented as wires with smooth boundaries; the ratio of the length to the width was greater than 20 and the width statistically decreased with decreasing thickness. To reveal the orientation of the KP_{15} nanoribbons, a high resolution TEM analysis was performed. Figure 3f shows that the longitudinal direction of the KP_{15} nanoribbon was parallel to the (1 1 0) plane. On the basis of the crystal structure and EDD information, KP_{15} is a layered structure with van der Waals

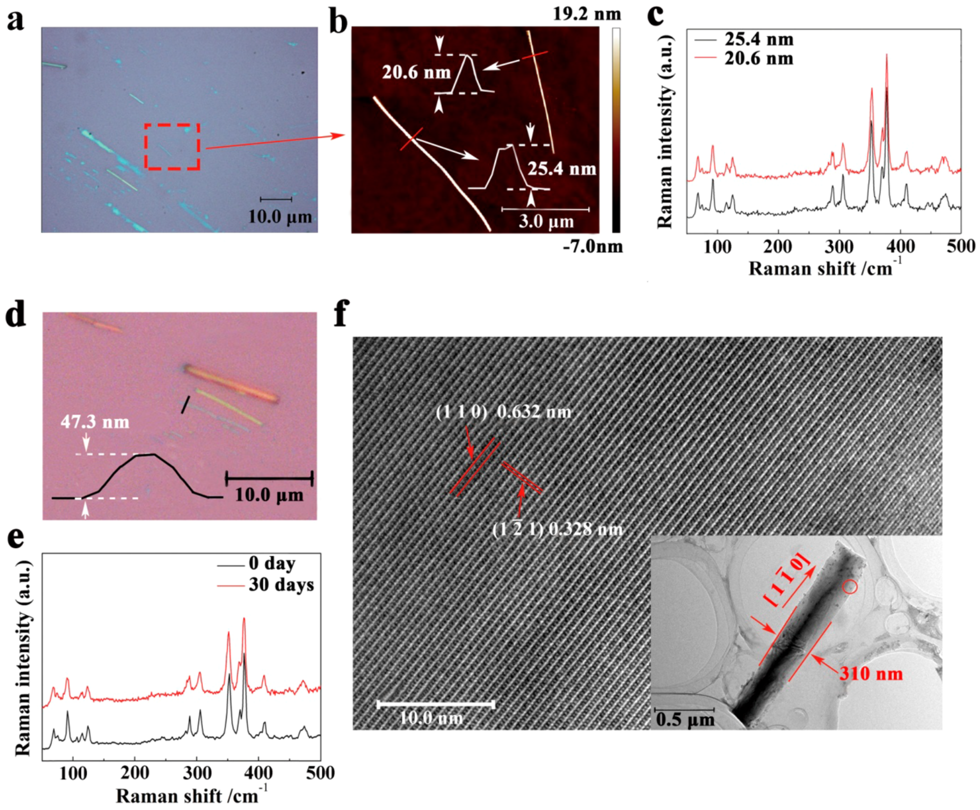

Figure 3. Characterization of KP$_{15}$ nanoribbon. (a) Optical micrograph of nanoribbons. (b) AFM results of nanoribbons shown in the square area marked in Figure 3a. (c) Raman results of the nanoribbons in (a). (d) Optical micrograph and AFM result of the 47.3 nm thick KP$_{15}$. (e) Raman result of a 47.3 nm KP$_{15}$ after exfoliation and after one month in ambient conditions. The tested sample is marked by a black line. (f) High resolution TEM image of a KP$_{15}$ nanoribbon prepared by wet transfer. Illustration at lower right is the corresponding bright field image, and the red circle marks the place where the high resolution image was taken.

forces connecting the layers, and the KP$_{15}$ nanoribbons were exfoliated by mechanical exfoliation. The orientation of the nanoribbons must lie in the (0 0 1) plane (Figure 1). In light of this, the longitudinal direction of the KP$_{15}$ nanoribbons was surely along [1 $\bar{1}$ 0], which was the direction of the P tubes. In addition, the chemical stability of the KP$_{15}$ nanoribbons was tested. A 47.3 nm thick KP$_{15}$ nanoribbon (Figure 3d) was placed under ambient conditions without any protection for one month. After normalization by the Si Raman signal at 521 cm^{-1}, the intensities and positions of the Raman peaks were apparently unchanged (Figure 3e), a finding which strongly indicates that KP$_{15}$ nanoribbons are stable under ambient conditions (theoretical discussion can be seen in Figure S4).

We also used angle-resolved polarized Raman configurations to study the anisotropy in exfoliated KP$_{15}$ and the results showed obvious anisotropy. We chose to rotate the laser polarization direction by a half-wave plate positioned in the incident laser path and set an analyzer in front of the spectrometer entrance to select polarization of the Raman signal parallel to the vertical axis. We defined the intersection angle between the laser polarization and laboratory vertical axis as θ. As labeled in Figure 4, the y-axis of the KP$_{15}$ sample, which is also the direction of a P tube, is placed along the laboratory vertical axis. The details of these angle-resolved polarized Raman configurations have been described elsewhere.[30] Two exfoliated KP$_{15}$ samples, one 116.4 nm thick and 373.9 nm wide and the other 111.9 nm thick and 2.3 μm wide, were chosen for Raman measurement. As shown sequentially in Figures 4b and 4e, 14 Raman peaks were, respectively, located at 466.6, 449.0, 408.8, 376.3, 368.4, 351.1, 303.7, 288.5, 124.1, 114.1, 106.8, 90.7, 74.6, and 66.4 cm^{-1}. The intensities of all the Raman peaks were sensitive to the laser polarization angle θ. For the two samples, when the laser polarization direction was parallel to the y-axis, the intensities of almost all the Raman peaks reached their maximum values, and when the laser polarization direction was perpendicular to the y-axis, the intensities of almost all the Raman peaks reached their minimum values. The angle-resolved Raman intensities of peak 9 are shown in Figure 4c and 4f for the two samples, respectively; the results of the other peaks are shown in Figure S5. For the 373.9 nm wide sample, the Raman intensities of all the peaks follow a function of $\cos^6 \theta$. However, for the 2.3 μm wide sample, the Raman intensities of almost the peaks are better fitted by $\cos^2 \theta$. To figure out the reason for the different behavior of Raman intensities in the two samples, another two samples with similar thickness but different widths (106.9 nm thick and 924.4 nm wide; 111.9 nm thick and 1.1 μm wide) were tested by angle-resolved Raman measurements (results are shown in Figure S5). Among these 4 samples, the three samples whose widths were greater than the excitation wavelength (488 nm) showed similar anisotropic Raman features. However, the Raman spectra of the 373.9 nm wide sample exhibited angular-dependent Raman intensities that were quite different from those of the other three samples.

The Raman scattering intensity of a Raman-active mode can be expressed as $\sum_j |\mathbf{e}_s \mathbf{R}_j \mathbf{e}_i|^2$, in which $\mathbf{R}_j$ is the Raman tensor of a certain Raman active mode and $\mathbf{e}_i$ and $\mathbf{e}_s$ are the unit polarization vectors of the incident laser and the scattered

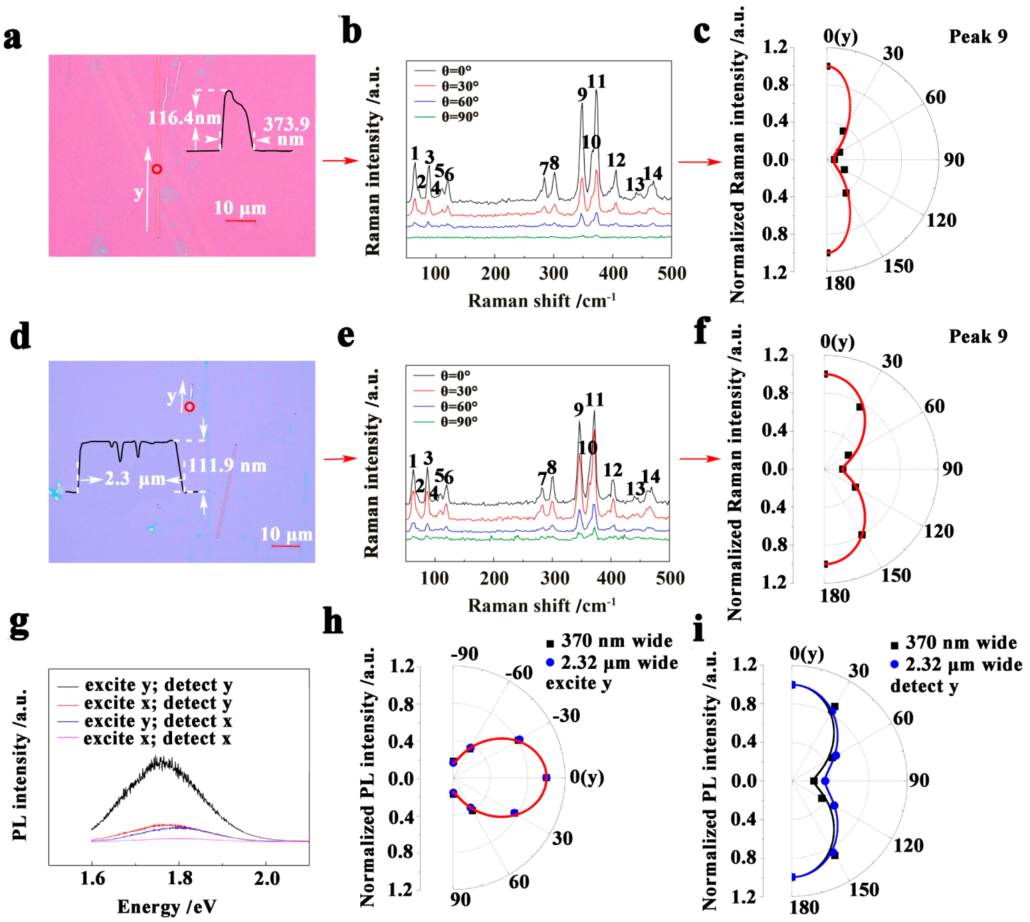

Figure 4. Anisotropic Raman response and photoluminescence of the exfoliated KP_{15}. (a) Optical micrograph and AFM result for the KP_{15} nanoribbon (116.4 nm thick, 373.9 nm wide) on a SiO_2/Si substrate. The tested nanoribbon is marked by a red circle. (b) Angle-resolved polarized Raman spectra of the KP_{15} nanoribbon (116.4 nm thick, 373.9 nm wide) excited by 488 nm laser. θ is the intersection angle between the laser polarization and laboratory vertical axis. KP_{15} nanoribbons placed with its y-axis along the laboratory vertical axis. The Raman peaks are labeled sequentially. (c) Normalized Raman intensity of peak 9 as a function of θ, KP_{15} nanoribbon is 116.4 nm thick, 373.9 nm wide. (d) Optical image and AFM result for the KP_{15} microribbon (111.9 nm thick, 2.3 μm wide) on a SiO_2/Si substrate. The tested microribbon is marked by a red circle. (e) Angle-resolved polarized Raman spectra of the KP_{15} microribbon (111.9 nm thick, 2.3 μm wide) excited by 488 nm laser. (f) Normalized Raman intensity of peak 9 as a function of θ, KP_{15} nanoribbons is 111.9 nm thick, 2.3 μm wide. Red circles in Figures 4a and 4d mark the place where the Raman and PL data was collected. (g) Polarization-resolved PL intensity for the 116.4 nm thick KP_{15} (373.9 nm wide). (h) Photoluminescence peak intensity as a function of the detection angle θ. (i) Photoluminescence peak intensity as a function of excitation angle θ (solid lines are fitted curves using a $\cos^2\theta$ function).

Raman signal, respectively. The space group of KP_{15} is $P\bar{1}$ and the corresponding point group is Ci. There is only one kind of irreducible representation, and the corresponding Raman tensor is $\begin{pmatrix} a & d & e \\ d & b & f \\ e & f & c \end{pmatrix}$. According to the angle-resolved polarized Raman configurations used here, $\mathbf{e}_i^T$ can be set to $(\sin\theta\ \cos\theta\ 0)$ and $\mathbf{e}_s$ can be set to $(0\ 1\ 0)$. KP_{15} is a layered material and the longitudinal direction of the KP_{15} nanoribbons is along $[1\ \bar{1}\ 0]$, So the Raman tensor $(\mathbf{R}_j)$ must be converted into the laboratory coordinates $(\mathbf{R}_j')$ by $\mathbf{R}_j' = \mathbf{M}\cdot\mathbf{R}_j\cdot\mathbf{M}^T$. $\mathbf{M} = \begin{pmatrix} \cos\delta & \sin\delta & 0 \\ -\sin\delta & \cos\delta & 0 \\ 0 & 0 & 1 \end{pmatrix}$ $(\delta = 90° - 63.696991° = 26.303009°$ where 63.696991 is the intersection angle between $[1\ 0\ 0]$ and $[1\ -1\ 0]$). Thus, the Raman intensity of the Raman mode should be $\{\sin\theta\,[d\cos^2\delta - d\sin^2\delta + (b-a)\cos\delta\sin\delta] + \cos\theta[b\cos^2\delta + a\sin^2\delta - 2d\cos\delta\sin\delta]\}^2$. For the three samples whose widths were greater than the excitation wavelength (488 nm), their angle-resolved polarized Raman intensities of peak 9 can be approximately fitted by $\cos^2\theta$, which indicates that $d\cos^2\delta - d\sin^2\delta + (b-a)\cos\delta\sin\delta]$ is close to 0. On the basis of that, if the orientation of the KP_{15} samples have changed, value of δ will change. That will make the change regulations of the Raman peak change. However, for the 373.9 nm wide one, the Raman intensity showed a distinct relationship to $\cos^6\theta$. One possible explanation for its different behavior could be the dielectric shape effect.[31,32] When the width of a nanoribbon is smaller than the excitation wavelength, the electric field inside the nanoribbon will be attenuated when the polarization direction of the excitation laser is perpendicular to the nanoribbon. Combining the dielectric shape effect with the intrinsic anisotropy may lead to the different angle-resolved Raman intensities for the 373.9 nm wide one. The width (2.3 μm) of the 111.9 nm thick sample was greater than the excitation wavelength, so the dielectric shape effect could be ignored. Regardless of whether the ribbon widths were less or greater than the excitation wavelength, all the KP_{15} samples exhibited significant anisotropy in the Raman intensities in the angle-resolved polarized Raman measurements. This reveals the intrinsic anisotropy of lattice structure of KP_{15}. Therefore, it is expected that polarized Raman measurements can be effective for quickly determining the *y*-axis orientation of bulk KP_{15}.

The exfoliated KP_{15} not only has anisotropic Raman features but also has anisotropic photoluminescence properties that are similar to phosphorene.[16] The results of a polarization-resolved photoluminescence study of the 373.9 nm wide and 2.3 μm wide KP_{15} samples are shown in Figure 4g–i. The photoluminescence intensity of the 373.9 nm wide and 2.3 μm wide samples as a function of the detection angle θ are shown in Figure 4g, 4h. The intensities of the emission peaks detected along the *y*-axis were 5.8 times those detected along the *x*-axis when the laser polarization was kept constant. A similar tendency was found for the 2.3 μm wide KP_{15} sample. This implies that the high anisotropic emission property comes from its high anisotropic structure. In addition, to discover the origin of the excited states, the PL intensity dependence of the excitation power (Figure S6) was measured. According to earlier research, if $I \propto P^{\alpha}$ (α is between 1 and 2; I is the PL peak intensity and P is the excitation power), localized states may be the origin of the emission.[33,34] If $I \propto P^{0.5}$, the emission can be dominated by the recombination of localized electron–hole pairs.[35] If $I \propto P^{0.8}$, the excitons bound to defects may be the origin of the emission.[33] If $I \propto P$, the recombination of excitons is the primary origin.[34,36,37] Here, in our experiment (Figure S6), the emission intensity was linearly dependent on the excitation power, so the observed high anisotropic PL properties of KP_{15} are dominated by exciton recombination. On the basis of a first-principles calculation, the mobility for KP_{15} is also anisotropic. For both electron and hole, μ_y is 1 order of magnitude larger than μ_x. (μ_y: the mobility along the P tube, μ_x: the mobility perpendicular to the P tube;).[38] The EDD extends along the phosphorus tubes and separates along the direction perpendicular to the phosphorus tubes (as shown in Figures 2 and S3). Thus, the carriers are more mobile along the phosphorus tubes than perpendicular to it. In addition, highly anisotropic moving carriers form anisotropic excitons, leading to a high anisotropic emission.[16] Moreover, the observed exciton emission at room temperature means that KP_{15} has a high exciton binding energy.

Also, the emission intensity of the KP_{15} samples depends on the polarization of the excitation light. The photoluminescence intensity of the 373.9 nm wide and 2.3 μm wide samples as a function of the excitation angle θ is shown in Figure 4i. For the 116.4 nm thick nanoribbon (373.9 nm wide), the photoluminescence intensity when the polarization of excited light was along the *y*-axis (I_y) was 4.34 times the intensity when the polarization of excited light was along the *x*-axis (I_x) (polarization ratio was 0.23 with polarization ratio defined as I_x/I_y). However, for the 111.9 nm thick microribbon (2.3 μm wide), the photoluminescence intensity when the polarization of excited light was along the *y*-axis was 2.88 times the intensity when the polarization of excited light was along the *x*-axis (polarization ratio was 0.35). Two additional samples with similar thicknesses and different widths (106.9 nm thick and 924.4 nm wide; 111.9 nm thick and 1.1 μm wide) were tested by angle-dependent PL (results shown in Figure S7). Of those 4 samples, the three samples in which the widths were greater than the wavelength of the excitation light (532 nm) showed similar anisotropic excitation, but the 373.9 nm wide one differed from the others. The polarization ratio of the 373.9 nm wide sample was smaller than that of other three samples whose widths were greater than the excitation wavelength (532 nm). This difference in anisotropic excitation could have been caused by the size effect. The 116.4 nm thick sample with a large aspect ratio can be considered to be a quasi-one-dimensional material in that it had a width that was less than the excitation wavelength. In this situation, when the polarization of an excitation laser was perpendicular to the length of a nanoribbon, the electric field inside the nanoribbon was reduced,[31,39,40] leading to a smaller polarization ratio. However, the 111.9 nm thick microribbon that had a width greater than the excited wavelength (532 nm) did not show any size effect in the anisotropic excitation, so the observed anisotropic excitation of this sample may reveal the intrinsic anisotropic excitation characteristics of KP_{15}. Meanwhile, the PL intensity depends on the absorption and internal quantum efficiency. Only the absorption depends on the excitation laser polarization; thus, the absorption of KP_{15} is anisotropic and the calculated result also showed anisotropic absorption (as shown in Figure S8).

CONCLUSIONS

In summary, a highly anisotropic electron density distribution and a fiber-like layered crystal structure were identified for KP_{15}. Good chemical stability, anisotropic emission performance, and high exciton binding energy offer great advantages for discovering unusual many-body physical phenomena and that may also impact the development of high-performance optoelectronic and photonic devices, such as anisotropic optical detectors or on-chip optical interconnects.

The high anisotropic properties in KP_{15} have been investigated. However, there is still a lot of work that should be done in the future. The vibrational properties, carrier mobilities, absorptivities, and the exciton properties in KP_{15} still need experimental investigation. Meanwhile, chain-like structure and ribbon-like exfoliated KP_{15} sample indicate that KP_{15} may be prepared to one-dimensional material. Preparation and investigation of quasi-one-dimensional KP_{15} are still full of challenges.

METHODS

Sample Preparation. Potassium (0.130 g, 97%) and red phosphorus (1.370 g, 99.9999%) were mixed in a vacuum quartz tube (the atomic proportion of potassium was 7%). Next, the quartz tube was heated for 12 h with a temperature gradient of 650 °C/200 °C, similar to the report by Schenering *et al.*[21] After that, needle-like dark red KP_{15} crystals could be seen in the middle of the quartz tubes. Nano- and microscale KP_{15} samples were prepared by mechanical exfoliation. SiO_2 (300 nm)/Si substrates were successively ultrasonically cleaned by oxygen plasma for 1 min to remove any adsorbates on the surface of the substrates. Next, commercially available 3 M cellophane tape was used to pick up the samples. Finally, the sample-loaded tapes were brought into contact with the substrate. Before removing the tape, the substrates were annealed at 100 °C for 2 min in air. A TEM sample was prepared using a wetting transfer technology. After mechanical exfoliation, a thin film of PMMA was spin-coated onto the SiO_2(300 nm)/Si substrate; then a 1 mol L^{-1} KOH hot solution was used to remove the SiO_2 layer, separating the KP_{15} samples and the PMMA from the SiO_2/Si. The PMMA containing the KP_{15} samples was carefully moved to carbon micro grids. After annealing, acetone was used to remove the PMMA, leaving the KP_{15} samples on the carbon micro grids.

Single-Crystal XRD Measurements, Refinement of the Crystal Structure, and MEM Calculation. Single-crystal diffraction data was collected at room temperature using a Rigaku supernova single crystal diffractometer (Cu $K_{\alpha 1}$ radiation; $\lambda = 1.54184$ Å; graphite monochromator). The final crystal information was refined using the SHELXL-97 package.

EDS and XPS Measurements. The EDS result was collected using a JEOL JSM 6500F SEM, the SEM image was collected using an FEI Quanta 250 SEM. The XPS data was collected using a Thermo ESCALAB 250Xi XPS at Beijing ZKBC Testing and Technology Co., Ltd.

MEM and First-Principles Calculations. The VESTA and RainbowMEM-v1.7.2 program packages were applied in the MEM calculation based on single diffraction data of KP_{15}. First-principles calculations were performed using the Vienna *ab initio* simulation package (VASP).[41] The potentials used to characterize the elements were constructed by the projector augmented wave (PAW),[42] and the exchange-correlation part of the density functional was treated within the generalized gradient approximation of Perdew−Burke−Ernzerhof (GGA-PBE).[43,44] The cutoff energy for the plane-wave basis was 500 eV. Monkhorst−Pack k-points,[45] which mesh with a Gaussian smearing of 0.05 eV, were used to sample the Brillouin zones. Convergence with respect to self-consistent iterations was assumed when the total energy difference between cycles was $<1.0 \times 10^{-6}$ eV atom^{-1} and the residual forces were <0.01 eV Å^{-1}. To optimize the system geometry, van der Waals interactions were considered by the Tkatchenko and Scheffler (TS) approach.[46] Compared with the experimental results, our optimized structure parameters show excellent agreement (as shown in Table S4).

TEM Measurement and AFM Measurements. The TEM analysis was carried out using a JEOL JEM-2100 operated at 200 kV accelerating voltage. A Bruker MultiMode 8 SPM system utilizing the ScanAsyst mode was used to identify the sizes of the KP_{15} nanoribbons in an ambient environment at room temperature.

Raman, Polarized Raman Measurements. Raman and angle-resolved polarized Raman experiments on KP_{15} nanoribbons were performed on a HORIBA Jobin Yvon LabRAM HR Evolution system in an ambient environment at room temperature. The excitation wavelength was 488 nm and each spot size was about 1−2 μm. The incident laser polarization was changed from vertical polarization by rotating the fast axis of the half-wave plate positioned in the incident laser path. We defined the intersection angle between the laser polarization and laboratory vertical axis as θ. An analyzer was set in front of the spectrometer entrance to obtain the polarization of the Raman signal parallel to the vertical axis. To avoid possible heat damage, the laser power was kept below 25 μw. The excitation laser power was kept constant. The integral times were both 60 s.

Polarization-Resolved Photoluminescence Measurements and PL Intensity Depending on Excitation Power Measurement. Additional PL intensity measurements that depended on the excitation power and their corresponding Raman measurements were all measured using a WITec alpha300 RA confocal Raman microscopy system at room temperature. The excitation wavelength was 532 nm and the spot size was about 500 nm. The incident laser polarization was changed from vertical polarization by rotating the fast axis of the half-wave plate positioned in the incident laser path. During polarization-resolved photoluminescence measurements, one polarizer was used on the detection side to obtain different polarization of the emission signal. After being selected by the polarizer, the emission signal was transferred to the spectrometer by a multimode optical fiber. The laser power was kept at 23 μw and the integral times were 10 s. During the PL intensity depending on the excitation power measurement, the polarization of the laser was always along the longitudinal direction of the KP_{15} nanoribbons and no polarizer was used on the detection side.

ASSOCIATED CONTENT

Supporting Information

The Supporting Information is available free of charge on the ACS Publications website at DOI: 10.1021/acsnano.7b08368.

Crystallographic information file of KP_{15} (CIF)
Additional crystal information, XPS result, Raman, PL results and the theoretical results (PDF)

AUTHOR INFORMATION

Corresponding Authors

*E-mail: dmliu@bjut.edu.cn.
*E-mail: yzzhang@bjut.edu.cn.

ORCID

Danmin Liu: 0000-0002-4031-1351
Ping-Heng Tan: 0000-0001-6575-1516
Yongzhe Zhang: 0000-0002-3471-4402

Author Contributions

∇NT and YY contributed equally.

Notes

The authors declare no competing financial interest.

ACKNOWLEDGMENTS

This work was supported by the National Natural Science Foundation of China (NSFC 51671006 and 61575010), the Natural Science Foundation of Beijing (4162016) and the Science and Technology Commission of Beijing Municipality (Z151100003315018). The authors appreciate the very extensive grammar and content editing by and helpful discussions with Edmund F. and Rhoda E. Perozzi, PhDs.

ABBREVIATIONS

EED, electron-density distribution; MEM, maximum entropy method

REFERENCES

(1) Novoselov, K. S.; Geim, A. K.; Morozov, S. V.; Jiang, D.; Katsnelson, M. I.; Grigorieva, I. V.; Dubonos, S. V.; Firsov, A. A. Two-Dimensional Gas of Massless Dirac Fermions in Graphene. *Nature* **2005**, *438*, 197−200.

(2) Novoselov, K. S.; Geim, A. K.; Morozov, S. V.; Jiang, D.; Zhang, Y.; Dubonos, S. V.; Grigorieva, I. V.; Firsov, A. A. Electric Field Effect in Atomically Thin Carbon Films. *Science* **2004**, *306*, 666−669.

(3) Zhang, B. Y.; Liu, T.; Meng, B.; Li, X.; Liang, G.; Hu, X.; Wang, Q. J. Broadband High Photoresponse from Pure Monolayer Graphene Photodetector. *Nat. Commun.* **2013**, *4*, 1811−1822.

(4) Bonaccorso, F.; Sun, Z.; Hasan, T.; Ferrari, A. C. Graphene Photonics and Optoelectronics. *Nat. Photonics* **2010**, *4*, 611−622.

(5) Xia, F.; Mueller, T.; Lin, Y.; Valdesgarcia, A.; Avouris, P. Ultrafast Graphene Photodetector. *Nat. Nanotechnol.* **2009**, *4*, 839−843.

(6) Ellis, J. K.; Lucero, M. J.; Scuseria, G. E. The Indirect to Direct Band Gap Transition in Multilayered MoS2 as Predicted by Screened Hybrid Density Functional Theory. *Appl. Phys. Lett.* **2011**, *99*, 261908.

(7) Wang, Q. H.; Kalantar-Zadeh, K.; Kis, A.; Coleman, J. N.; Strano, M. S. Electronics and Optoelectronics of Two-Dimensional Transition Metal Dichalcogenides. *Nat. Nanotechnol.* **2012**, *7*, 699−712.

(8) Lopezsanchez, O.; Lembke, D.; Kayci, M.; Radenovic, A.; Kis, A. Ultrasensitive Photodetectors Based on Monolayer MoS2. *Nat. Nanotechnol.* **2013**, *8*, 497−501.

(9) Alem, N. Atomically Thin Hexagonal Boron Nitride Probed by Ultrahigh-Resolution Rransmission Electron Microscopy. *Phys. Rev. B: Condens. Matter Mater. Phys.* **2009**, *80*, 155425.

(10) Dean, C. R.; Young, A. F.; Meric, I.; Lee, C.; Wang, L.; Sorgenfrei, S.; Watanabe, K.; Taniguchi, T.; Kim, P.; Shepard, K. L. Boron Nitride Substrates for High-Quality Graphene Electronics. *Nat. Nanotechnol.* **2010**, *5*, 722−726.

(11) Song, L.; Liu, Z.; Reddy, A. L.; Narayanan, N. T.; Taha-Tijerina, J.; Peng, J.; Gao, G.; Lou, J.; Vajtai, R.; Ajayan, P. M. Binary and Ternary Atomic Layers Built from Carbon, Boron, and Nitrogen. *Adv. Mater.* **2012**, *24*, 4878−4895.

(12) Cao, W.; Kang, J.; Sarkar, D.; Liu, W. 2D Semiconductor FETs—Projections and Design for Sub-10 nm VLSI. *IEEE Trans. Electron Devices* **2015**, *62*, 3459−3469.

(13) Tran, V.; Yang, L. Scaling Laws for The Band Gap and Optical Response of Phosphorene Nanoribbons. *Phys. Rev. B: Condens. Matter Mater. Phys.* **2014**, *89*, 106−114.

(14) Nemilentsau, A.; Low, T.; Hanson, G. Anisotropic 2D Materials for Tunable Hyperbolic Plasmonics. *Phys. Rev. Lett.* **2016**, *116*, 066804.

(15) Ali, M. N.; Xiong, J.; Flynn, S.; Tao, J.; Gibson, Q. D.; Schoop, L. M.; Liang, T.; Haldolaarachchige, N.; Hirschberger, M.; Ong, N. P. Large, Non-saturating Magnetoresistance in WTe2. *Nature* **2014**, *514*, 205−208.

(16) Wang, X.; Jones, A. M.; Seyler, K. L.; Tran, V.; Jia, Y.; Zhao, H.; Wang, H.; Yang, L.; Xu, X.; Xia, F. Highly Anisotropic and Robust Excitons in Monolayer Black Phosphorus. *Nat. Nanotechnol.* **2014**, *10*, 517−521.

(17) Liu, F.; Zheng, S.; He, X.; Chaturvedi, A.; He, J.; Chow, W. L.; Mion, T. R.; Wang, X.; Zhou, J.; Fu, Q. Highly Sensitive Detection of Polarized Light Using Anisotropic 2D ReS2. *Adv. Funct. Mater.* **2016**, *26*, 1146−1146.

(18) Xia, F.; Wang, H.; Jia, Y. Rediscovering Black Phosphorus as An Anisotropic Layered Material for Optoelectronics and Electronics. *Nat. Commun.* **2014**, *5*, 289−305.

(19) Liu, E.; Fu, Y.; Wang, Y.; Feng, Y.; Liu, H.; Wan, X.; Zhou, W.; Wang, B.; Shao, L.; Ho, C. H. Integrated Digital Inverters Based on Two-Dimensional Anisotropic ReS2 Field-Effect Transistors. *Nat. Commun.* **2015**, *6*, 6991−6998.

(20) Favron, A.; Gaufrès, E.; Fossard, F.; Lévesque, P. L.; Phaneufl'Heureux, A.; Tang, N. Y.; Loiseau, A.; Leonelli, R.; Francoeur, S.; Martel, R. Exfoliating Pristine Black Phosphorus Down to The Monolayer: Photo-Oxidation and Electronic Confinement Effects. *Physics* **2014**, *1*, 708−712.

(21) Schenering, H. G. V.; Schmidt, D. C. H. KP15, A New Potassium Polyphosphide. *Angew. Chem., Int. Ed. Engl.* **1967**, *6*, 356−356.

(22) Olego, D. J. Vibrational and Electronic Properties of MP15 Polyphosphides: Crystalline RbP15, KP15, and NaP15. *Phys. Rev. B: Condens. Matter Mater. Phys.* **1985**, *31*, 2230−2239.

(23) Schachter, R.; Michel, C. G.; Kuck, M. A.; Baumann, J. A.; Olego, D. J.; Polgar, L. G.; Raccah, P. M.; Spicer, W. E. Semiconductor Properties of Polyphosphides. *Appl. Phys. Lett.* **1984**, *45*, 277−279.

(24) Cheon, G.; Duerloo, K. N.; Sendek, A. D.; Porter, C.; Chen, Y.; Reed, E. J. Data Mining for New Two- and One-Dimensional Weakly Bonded Solids and Lattice-Commensurate Heterostructures. *Nano Lett.* **2017**, *17*, 1915−1923.

(25) Huang, X.; Guan, J.; Lin, Z.; Liu, B.; Xing, S.; Wang, W.; Guo, J. Epitaxial Growth and Band Structure of Te Film on Graphene. *Nano Lett.* **2017**, *17*, 4619−4623.

(26) Mihailovic, D. Inorganic Molecular Wires: Physical and Functional Properties of Transition Metal Chalco-Halide Polymers. *Prog. Mater. Sci.* **2009**, *54*, 309−350.

(27) Zhu, Z.; Cai, X.; Niu, C.; Yi, S.; Guo, Z.; Liu, F.; Cho, J. H.; Jia, Y.; Zhang, Z. Density-Functional Calculations of Multivalency-Driven Formation of Te-Based Monolayer Materials with Superior Electronic and Optical Properties. *Phys. Rev. Lett.* **2017**, *119*, 106101.

(28) Sakata, M.; Sato, M. Accurate Structure Analysis by The Maximum-Entropy Method. *Acta Crystallogr., Sect. A: Found. Crystallogr.* **1990**, *46*, 263−270.

(29) Jauch, W.; Palmer, A. The Maximum-Entropy Method in Charge-Density Studies: Aspects of Reliability. *Acta Crystallogr., Sect. A: Found. Crystallogr.* **1993**, *49*, 590−591.

(30) Liu, X. L. Different Angle-Resolved Polarization Configurations of Raman Spectroscopy: A Case on The Basal and Edge Plane of Two-Dimensional Materials. *Chin. Phys. B* **2017**, *26*, 422−429.

(31) Wang, J.; Gudiksen, M. S.; Duan, X.; Cui, Y.; Lieber, C. M. Highly Polarized Photoluminescence and Photodetection from Single Indium Phosphide Nanowires. *Science* **2001**, *293*, 1455−1457.

(32) Schafer-Nolte, E. O.; Stoica, T.; Gotschke, T.; Limbach, F. Highly Polarized Raman Scattering Anisotropy in Single GaN Nanowires. *Appl. Phys. Lett.* **2010**, *96*, 091907.

(33) Luckert, F.; Yakushev, M. V.; Faugeras, C.; Karotki, A. V.; Mudryi, A. V.; Martin, R. W. Excitation Power and Temperature Dependence of Excitons in CuInSe2. *J. Appl. Phys.* **2012**, *111*, 093507.

(34) Chiari, A.; Colocci, M.; Fermi, F.; Li, Y. H.; Querzoli, R.; Vinattieri, A.; Zhuang, W. H. Temperature-Dependence of the Photoluminescence in GaAs-GaAlAs Multiple Quantum Well Structures. *Phys. Status Solidi B* **1988**, *147*, 421−429.

(35) Brener, I.; Olszakier, M.; Cohen, E.; Ehrenfreund, E.; Ron, A.; Pfeiffer, L. Particle Localization and Phonon Sidebands in GaAs/ Al x Ga 1 − x As Multiple Quantum Wells. *Phys. Rev. B: Condens. Matter Mater. Phys.* **1992**, *46*, 7927.

(36) Huang, J.; Hoang, T. B.; Mikkelsen, M. H. Probing the Origin of Excitonic States in Monolayer WSe2. *Sci. Rep.* **2016**, *6*, 22414.

(37) You, Y.; Zhang, X.-X.; Berkelbach, T. C.; Hybertsen, M. S.; Reichman, D. R.; Heinz, T. F. Observation of Biexcitons in Monolayer WSe2. *Nat. Phys.* **2015**, *11*, 477−481.

(38) Yanhan, Y.; Nan, T.; Yongzhe, Z.; Danmin, L.; Dong, Z.; Kai, C.; Hui, Y. Rediscovering MP15 Family (M = Li, Na, and K) as An Anisotropic Layered Semiconducting Material. *J. Phys. Chem. Lett.* **2017**, DOI: 10.1021/acs.jpclett.7b02817.

(39) Gudiksen, M. S.; Wang, J.; Lieber, C. M. Size-Dependent Photoluminescence from Single Indium Phosphide Nanowires. *J. Phys. Chem. B* **2002**, *106*, 4036−4039.

(40) Shan, C. X.; Liu, Z.; Hark, S. K. Photoluminescence Polarization in Individual CdSe Nanowires. *Phys. Rev. B: Condens. Matter Mater. Phys.* **2006**, *74*, 2952−2961.

(41) Kresse, G.; Furthmüller, J. Efficient Iterative Schemes for Ab Initio Total-Energy Calculations Using A Plane-Wave Basis Set. *Phys. Rev. B: Condens. Matter Mater. Phys.* **1996**, *54*, 11169.

(42) Blochl, P. E.; Jepsen, O.; Andersen, O. K. Improved Tetrahedron Method for Brillouin-Zone Integrations. *Phys. Rev. B: Condens. Matter Mater. Phys.* **1994**, *49*, 16223.

(43) Perdew, J. P. Accurate and Simple Density Functional for the Electronic Exchange Energy: Generalized Gradient Approximation. *Phys. Rev. B: Condens. Matter Mater. Phys.* **1986**, *33*, 8800−8802.

(44) Perdew, J. P.; Burke, K.; Ernzerhof, M. Generalized Gradient Approximation Made Simple. *Phys. Rev. Lett.* **1996**, *77*, 3865−3868.

(45) Monkhorst, H. J. Special Points for Brillouin-Zone Integrations. *Phys. Rev. B: Condens. Matter.* **1977**, *16*, 1748−1749.

(46) Tkatchenko, A.; Scheffler, M. Accurate Molecular Van Der Waals Interactions from Ground-State Electron Density and Free-Atom Reference Data. *Phys. Rev. Lett.* **2009**, *102*, 073005.